Full Adaptive Optics Images of Asteroids Ceres and Vesta; Rotational Poles and Triaxial Ellipsoid Dimensions[1]

Jack D. Drummond, Robert Q. Fugate, and Julian C. Christou

Starfire Optical Range, Air Force Research Laboratory, 3550 Aberdeen Ave SE, Kirtland AFB, New Mexico 87117-5776
E-mail: drummond@plk.af.mil

and

E. Keith Hege

Steward Observatory, University of Arizona, Tucson, Arizona 85721

Adaptive optics (AO) images of asteroids Ceres and Vesta were obtained on September 18–20, 1993, with the 1.5-m telescope at the Starfire Optical Range of the USAF Phillips Laboratory located near Albuquerque, NM. The light source for higher-order wavefront correction was a Rayleigh laser beacon focused at a range of 10.5 km generated by a copper vapor laser. On April 27 and May 11, 1996, Vesta was again imaged, this time at its perihelic opposition using Vesta itself as the beacon for the AO. Images obtained at an effective wavelength of 0.85 μm were analyzed with a new reconstruction technique, called parametric blind deconvolution. The technique allows fits for relevant parameters in the frequency domain, where the convolution of the asteroid ellipse with the variable Lorentz-shaped point spread function produced by the AO system during these observations can be separated into a multiplication of analytic functions.

The triaxial ellipsoid dimensions and rotational pole (with a two-fold ambiguity) of Ceres were obtained from 17 images and found to be in excellent agreement with its 1983 stellar occultation outline (Millis *et al.*, 1987, *Icarus* 72, 507–518) and the 1991 AO image produced by the COME-ON system (Saint-Pe *et al.*, 1993, *Icarus* 105, 271–281). A similar analysis of eight images of Vesta in 1993, 19 images in April 1996, and 28 images in May 1996, and combined with results from four previous speckle interferometry (SI) sets, yield dimensions and a rotational pole in reasonable agreement with the Hubble Space Telescope's results (Thomas *et al.* 1997). Differences may arise from a non-alignment between principal axes of inertia and the spin axis. The AO data from May 11, 1996, is of sufficient quality that Vesta's lightcurve can be decomposed into its cross-sectional area and surface brightness components, proving ana-lytically that Vesta's lightcurve minimum is caused by a dark hemisphere. Combining the AO and SI observations with previous lightcurves yields a sidereal period of 0.22258874 days with an uncertainty of 4 in the last decimal place (3.5 ms) and shows that lightcurve minimum occurs 6° before a maximum in cross-section area. © 1998 Academic Press

Key Words: imaging; adaptive optics; asteroids; rotational poles; dimensions; Ceres; Vesta.

1. INTRODUCTION

Laser guide star (lgs) Adaptive Optics (AO) images of Ceres and Vesta obtained with a 1.5-m telescope in September 1993, and natural guide star (ngs) AO images of Vesta in April and May 1996 have led to a determination of their triaxial dimensions and the directions of their spin vectors. The exceptional images of Vesta in May 1996 clearly show albedo markings that rotate across the face of the asteroid. For Ceres, we present the first direct measurement of a triaxial ellipsoid shape and the first pole estimate from observations spanning an entire rotational period. Drummond and Christou (1994) presented preliminary (and now superseded) results from the observations reported here. The results of Drummond (1995) and Drummond *et al.* (1996) are also slightly modified, mostly due to an improved pixel scale and orientation calibration.

The results reported here were obtained at the 1.5-m telescope of the Starfire Optical Range (SOR) located near Albuquerque, NM at the USAF Phillips Laboratory. The earliest versions of this system have been described by Fugate *et al.* (1993, 1994) and Fugate (1994). The current hardware configuration and recent experimental data are presented in the review by Roggeman *et al.* (1997) and by Glenar *et al.* (1997). Drummond *et al.* (1995) and Christou

et al. (1995) reported recent close binary star results from this system.

Dumas and Hainaut (1996a, 1996b) obtained AO images of Vesta, and Merline *et al.* (1996) obtained HST images of Ceres, but neither listed poles or dimensions. However, the detailed analysis of recent Vesta images from the Hubble Space Telescope (HST) (Thomas *et al.* 1997, Binzel *et al.* 1997, Zellner *et al.* 1997) invites us to compare our findings to theirs. In fact, HST images of Vesta obtained in 1996 were made between our April and May runs. We also compare our results for Ceres to the IR AO results of Saint Pe *et al.* (1993).

2. SYSTEM CONFIGURATION

The adaptive optics for the SOR 1.5-m telescope laser guide star system are located in a coudé room and consist of a 241 actuator continuous face-sheet deformable mirror, coarse and fine steering mirrors, two unintensified CCD based Shack–Hartmann wavefront sensors (one for natural objects and one for the copper vapor laser Rayleigh beacon), and a fiber optic synthesized 4×4 array of avalanche photo-diodes (Fugate *et al.* 1993) for tracking. When operating with the natural object wavefront sensor, the wavefront reconstructor can be configured as a full aperture tilt sensor, providing tilt error signals to an executive controller which drives the two steering mirrors and adjusts loop gain and compensation parameters. In this mode the full aperture tilt error signal is the mean tilt of the 208 higher-order wavefront sensor subapertures and in general provides better performance than the avalanche photo-diodes for natural objects bright enough for higher-order wavefront sensing. This was the principal mode of tracking for the 1996 observations of Vesta (V = 5.6).

In 1993 both asteroids were too faint (V = 8.0 for Ceres and 6.4 for Vesta) for high bandwidth, higher-order compensation, so an artificial star, a Rayleigh backscatter laser beacon, was used as a ''point'' source for the higher-order adaptive optics. The copper vapor laser operates at 5000 pulses per second at 50 ns per pulse with approximately 60 watts transmitted out the telescope. The laser shares the full aperture (necessitated by the low beam quality of the laser) of the telescope by means of a polarizing beam splitter and quarter-wave plate and is focused in the atmosphere at a range from the telescope of 10.5 km. The wavefront sensor is range-gated about a 1.2- to 2.4-km portion of the focused beam centered on 10.5 km. The high peak power of the laser pulses induces long lived phosphorescence in the optical components of the beam train which radiate in the passband of the photon-counting avalanche photo-diode track sensor, limiting tracking to 9th or 10th magnitude stars. This appears to be a fundamental limitation of this system. Images were recorded on a 512×512 thermoelectrically cooled Photometrics CCD

and all observations were obtained at an effective wavelength of 0.85 μm, with a passband of $\sim$0.2 μm.

The system evolved somewhat between the September 1993 and April 1996 observations, with the primary improvements being made in wavefront sensor gain and overall system stability (Pennington, 1995). We believe that image jitter is still the single biggest contributor to limiting system performance. A scoring camera independent of any track sensor has been used to characterize the power spectrum of the residual image jitter. These data lead to the discovery of strong structural resonances at 82 and 93 Hz in the four 1-in. diameter invar metering rods that despace the primary and secondary mirrors of the 1.5-m telescope. These 80- to 90-Hz disturbances are too high in frequency to be significantly attenuated by the control bandwidth of the tilt loop (which is estimated to be no more than 50 Hz for the signal available from Vesta).

3. OBSERVATIONS

The observing log and aspect data for both Ceres and Vesta are given in Table I. The positions of the asteroid, the solar phase angle, and the position angle of the Sun with respect to celestial north are adopted for the mean of the observations, but corrections were made to the scale in km/pixel for each night to account for the changing distance. *N* is the number of observations that were fit. The integration times for Ceres were 60 s, and for Vesta they were generally 20 s in 1993, 10 s in April 1996, and 3–4 s in May 1996.

The camera orientation and image scale were determined by four binaries in 1993 (0.0295 $\pm$ 0.0004″/pixel from γ Ari, ξ Cep, λ Ori, and γ Cet), three binaries in April 1996 (0.0678 $\pm$ 0.0001″/pixel from ξ Boo, 39 Dra, and ADS 9247), and 13 binaries in May 1996 (0.0689 $\pm$ 0.0006″/pixel). For the 1996 observations the CCD array was binned by two, hence the larger scale. The theoretical resolution for a 1.5-m telescope at 0.85 μm is 0.117″ so that the data was oversampled by $\sim$2$\times$ for the 1993 data and was approximately Nyquist sampled for the 1996 observations. All analysis was done on 128×128 pixel subarrays of the CCD, corresponding to fields of 3.8″ and 8.7–8.8″ for the 1993 and 1996 observations, respectively.

4. ASTEROID IMAGE ANALYSIS

While the purpose of AO systems is to increase the effective resolution from the atmospherically imposed limit of 1–2″ to that of the theoretical point spread function (PSF) appropriate for the telescope, this is seldom entirely achieved for a variety of reasons. For the SOR system as it existed for these observations, the main limitation to better performance was image motion jitter (of the order of 0.03″ rms) caused primarily by a 90-Hz resonance in

TABLE I
Observational Log and Aspect Data

Asteroid	Date	N	(2000.0)		Ecliptic		Phase angle	PA of Sun	$R_\odot$ (AU)	$R_\oplus$ (AU)	Scale (km/px)
			RA	Dec	Long.	Lat.					
Ceres	Sep. 18, 1993	7					13.4°		2.893	2.065	44.2
	Sep. 19	8	$2^h30.3^m$	+1°24′	36.0°	−11.8°	13.1	86.3°	2.892	2.056	44.0
	Sep. 20	2					12.8		2.892	2.047	43.8
Vesta	Sep. 18, 1993	2					11.3°		2.332	1.391	29.8
	Sep. 19	8†					11.7		2.333	1.398	29.9
	Sep. 20	6	$22^h23.0^m$	−20°53′	329.9°	−10.1°	12.1	229.9°	2.334	1.405	30.1
	† not used in fit										
Vesta	Apr. 27, 1996	19	$15^h27.2^m$	−7°14′	231.3°	+11.3°	8.2	66.4°	2.172	1.192	58.6
Vesta	May 11, 1996	28	$15^h14.1^m$	−6°43′	227.9°	+10.9°	5.2	0.0°	2.166	1.166	58.3

the telescope structure as mentioned above. Thus, AO compensated images only show partial corrections of atmospherically induced wavefront errors. Furthermore, as Drummond *et al.* (1995) and Christou *et al.* (1995) point out, AO PSFs are temporal, spatial, and object dependent, and therefore, AO compensated images of a reference star do not necessarily have the same PSF as a target object, in this case an asteroid.

In order to circumvent the PSF variability we have devised a scheme for extracting the parameteric information about an asteroid from the asteroid observation itself. We have found that the shape of the partially compensated PSF is well modeled by a Lorentzian for both the ngs and lgs observation modes. Comparison of a Lorentzian fit to an Airy pattern and to single and double Gaussians are shown in Figs. 1 and 2 for the lgs and ngs cases, respectively.

Making the usual assumptions for an asteroid, namely that it is a smooth, featureless, triaxial ellipsoid rotating about its shortest axis ($a \geq b \geq c$), then its image at any instant can be modeled as a flat-topped ellipse—an elliptical cylinder with a height of A_E corresponding to its albedo or mean surface brightness. The AO image of the asteroid is then the convolution of a flat-topped elliptical cylinder (the above atmosphere target) and a Lorentzian (the compensated PSF). The Fourier transform of this image is the product of the Fourier transform of the ellipse and the transform of the Lorentzian.

Since the Fourier transform of the observation is a product of two analytic functions in the frequency domain (see Appendix), it can be fit with a non-linear least squares routine that solves for the three parameters defining the Lorentzian (its semimajor axis, semiminor axis, and orientation), the four defining the flat-topped ellipse (the same parameters plus the asteroid's albedo), and the two locating the image center. Thus a simultaneous parameteric solution can be obtained for both the asteroid and the PSF without reference to an AO observation of a star taken at a different time and/or under different conditions. This

analysis is therefore similar to iterative blind deconvolution (IBD) in which the target and PSF are recovered from an observation making use of image constraints (support and non-negativity) and the convolution constraint (target and PSF estimates must convolve to the observation; Jefferies and Christou 1993). By using assumed shapes about both the target and PSF, we have been able to reduce the number of unknowns from $\sim 2N^2$, where N is the array side (typically ~ 128 in the IBD case) to just 9. We denote this technique parametric blind deconvolution (PBD). In addition, by constraining the object to be a uniform ellipse, we are able to extend the extraction of the asteroid parameters to cases where the asteroid is barely resolved, unlike the case for IBD which requires the first minimum of the Bessel function to be sampled in the Fourier domain (Christou *et al.* 1994).

The PBD approach finds analytic models for both the asteroid and its corresponding PSF. Departures of the asteroid from a uniform ellipse due to albedo variations or limb darkening, for example, can be (simply) investigated by examining the residuals from a linear deconvolution of the observation by the analytic PSF, i.e., the corresponding Lorentzian PSF fit. Albedo images, discussed later, are obtained by then convolving with an Airy function of the same FWHM as the Lorentzian. This suppresses the high-spatial frequency noise inherent in the Fourier quotient of the Lorentzian deconvolution. The "blurring" in the observations due to the extended wings of the Lorentzian is reduced by replacing a low Strehl ratio PSF with the "perfect" one. An Airy PSF is compared to a Lorentzian PSF of similar FWHM, i.e., that of the theoretical resolution limit, in Fig. 3 for the 1993 data. The Lorentzian has a FWHM of 4.07 pixels (0.12″), corresponding to a cut-off frequency of 31.5 pixels in the spatial–frequency domain. The Airy function, whose Fourier transform has this cut-off frequency, shows a FWHM of 4.13 pixels in the image domain. Assuming the Airy pattern has a Strehl ratio of unity, the Lorentzian then has a Strehl ratio of only $\sim 23\%$.
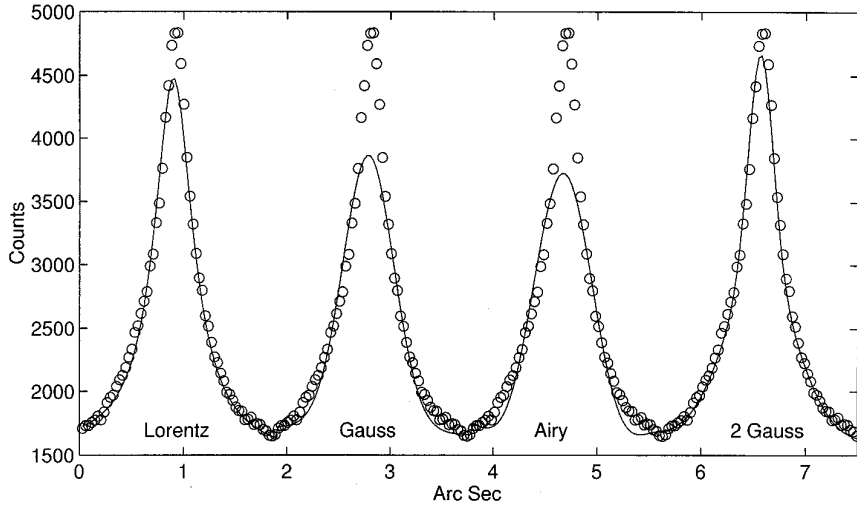
FIG. 1. Four functional fits to SAO 110603 on Sep. 19, 1993, observed with quad cell tracking to remove tip/tilt and high order compensation on a copper vapor laser guide star, i.e., laser guide star mode. Only a cut along a row is shown, but the standard error of fit over a 64 × 64 portion of the array was 55 counts for the Lorentzian fit, 100 for the single Gaussian, 183 for the Airy, and 52 for the double Gaussian. The G5 star of V mag 7.5 was difficult to track because of its faintness and the large background signal from the laser. This particular 60 s observation, typical of laser guide star work on a faint star, is from the second pair of asterisks in Fig. 7, just before 10 UT.

Thus, replacing the Lorentzian by the Airy pattern significantly enhances higher spatial frequencies in the image, albeit at the expense of some high frequency noise amplification.

The frequency domain fitting of the asteroid observation as the product of the Fourier transform of an ellipse and the transform of a Lorentzian is quite robust. The asteroid ellipse parameters do not depend very strongly on the region of fit, provided that not too much high spatial–frequency noise or signal from resolved structure is included. The size of the image sub-array over which the transform is made also has an impact on the fit, but this
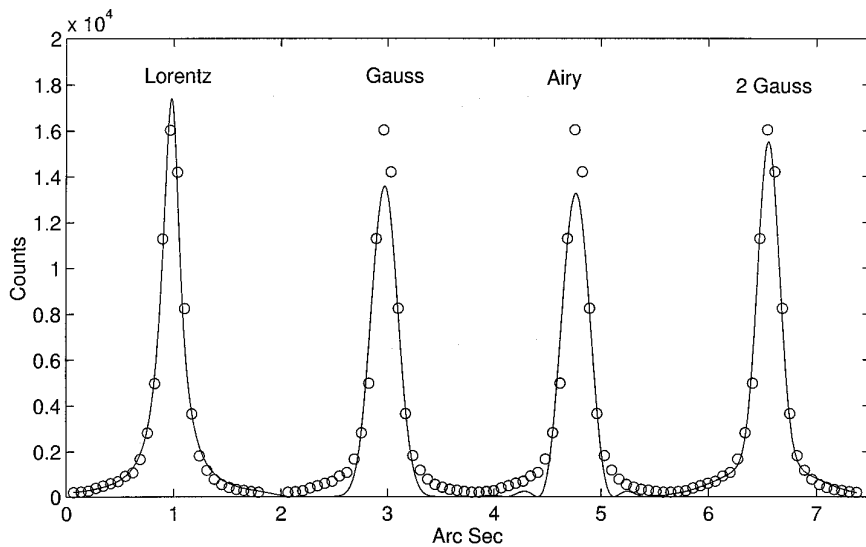

FIG. 2. Same as Fig. 1, except that the star is HR 5707 on May 11, 1996, in natural guide star mode. In this case the tracker is using the wave front sensor and the higher order corrections are made on the star itself. The K1 star is V mag 5.5, and the observation, 0.5 s long, is one of the pairs of asterisks just after 7 UT in Fig. 13. The standard error of fit over the 32 × 32 array for the Lorentzian fit was 190 counts, 424 for the single Gaussian, 437 for the Airy, and 194 for the double Gaussian.
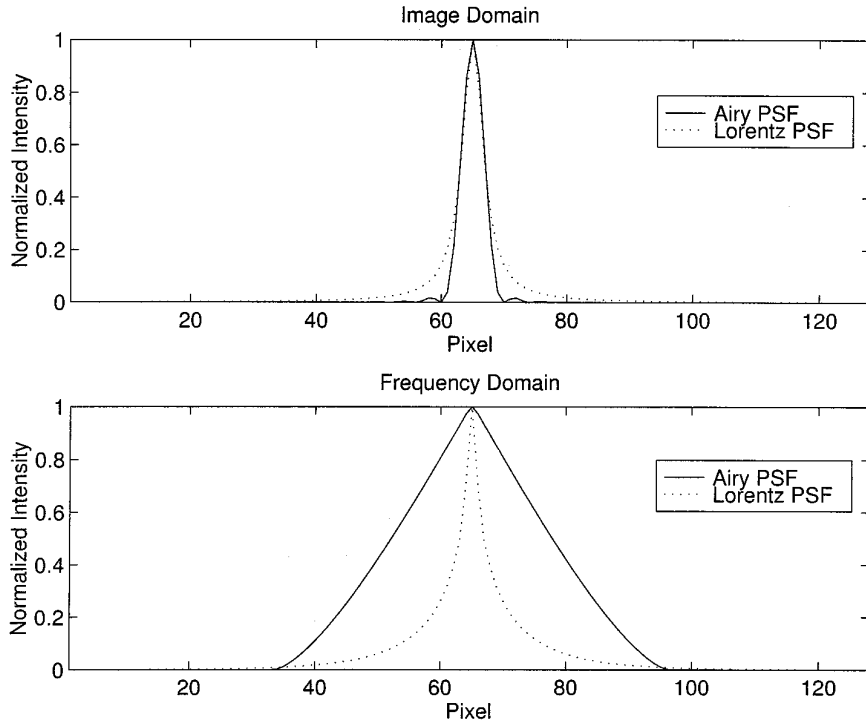
FIG. 3. Comparison of an Airy PSF to a Lorentzian PSF. The Airy PSF has a FWHM in the image domain of 4.13 pixels, appropriate for the image diffraction limit of 4.07 pixels (= 31.5 pixels in the frequency domain). The Lorentzian FWHM is 4.07 pixels, but only has a Strehl of 0.23.

can be minimized by giving lower weight to the lowest frequencies inside the first minimum of the Bessel pattern, including assigning zero weight to the center pixel or excluding it from the fit all together (see Appendix). Figure 4 shows a characteristic fit to an lgs observation of Ceres and Fig. 5 shows a fit to an ngs observation of Vesta in both image and frequency domains.

We compared the PBD analysis to more traditional deconvolution techniques for an image from the May 1996 Vesta data set by applying (a) an inverse filter linear deconvolution, (b) the non-linear techniques of Richardson–Lucy (RL), and (c) the conjugate gradient blind deconvolution (IBD), as well as (d) the PBD analysis. This is illustrated in Fig. 6, which compares the Fourier moduli and reconstructed images for the four techniques. The inverse filtering and RL analysis used a reference star for the PSF while the IBD and PBD were self-referencing, generating their own PSFs. The PBD results were obtained by deconvolving the observations by the Lorentzian PSF fit. As can be seen, there is a strong correlation between all four techniques, which suggests that the reference star PSF was actually a good match to the asteroid observations and that both IBD and PBD approaches are consistent. The benefit of fitting the very small number of parameters for the PDB analysis is thus justified. In all four cases the

reconstructed images are diffraction limited. Both IBD and PBD are further detailed in the Appendix.

5. RESULTS: TRIAXIAL ELLIPSOID DIMENSIONS AND ROTATIONAL POLES

5.1. Introduction

Using a known rotational period of 9.075 h for Ceres and 5.342 h for Vesta (Lagerkvist *et al.* 1989), the time of each observation is converted to a relative rotational phase with an arbitrary zero point. Each frequency domain fit generates nine parameters, four for the asteroid—its apparent ellipse major and minor axis dimensions (α_E, β_E), the position angle of the long axis (ω_E), and a mean surface brightness (A_E); three for the Lorentzian—α_L, β_L, and ω_L; and a center x_0 and y_0 for the image. As derived by Drummond *et al.* (1985a) and applied to asteroids by Drummond and Hege (1986, 1989), Drummond *et al.* (1985b, 1988a), and McCarthy *et al.* (1994), a series of such measurements of apparent ellipse parameters vs relative rotational phase leads to the triaxial ellipsoid dimensions and the three Euler angles necessary to define the direction of the spin axis. Two methods are used to make this transformation. One fits the apparent ellipse parameters α_E,
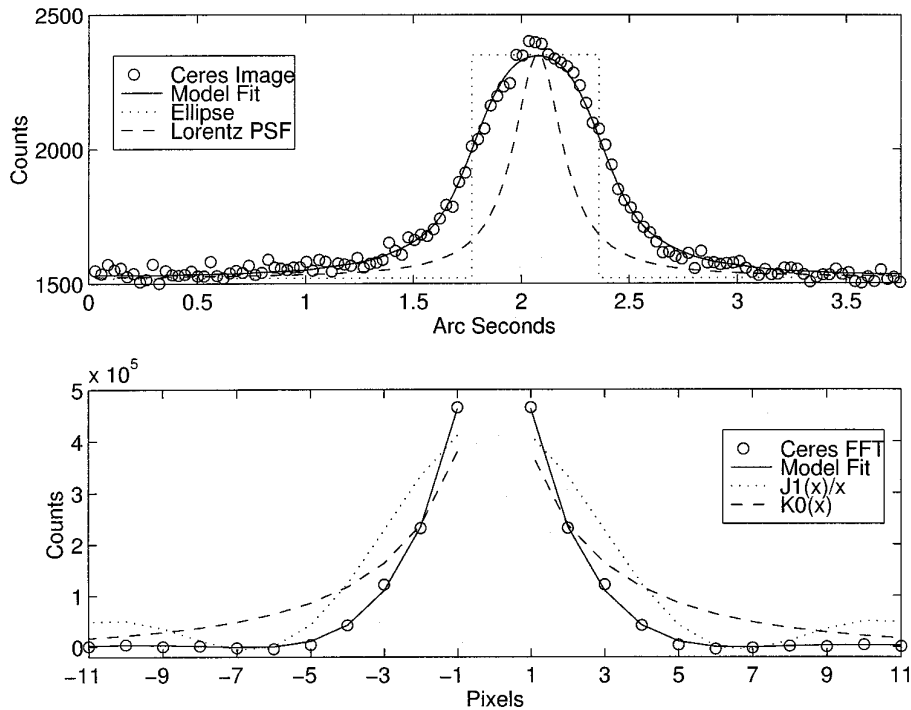
FIG. 4. Comparison of Ceres data to fits. Top figure shows a cut through the results, in the image domain, from the fit made in the frequency domain (bottom figure). In the image domain, the convolution of a flat-topped ellipse and a Lorentz PSF is the Fourier transform of the product, in frequency space, of a Bessel function divided by the radius of the ellipse, $2J_1(x)/x$, and a Hankel function, $K_0(x)$. The image plot shows the entire $3.8''$ field, but the frequency domain plot only shows the region of fit. Since a Hankel function is infinite at $x = 0$ in the frequency domain, the center pixel is not included in the fit. This particular data is from the next to last observation in Fig. 7, when the derived PSF was the smallest.

β_E, ω_E (Drummond *et al.* 1985a), and the other fits the X^2, Y^2, and XY moments of the ellipse (McCarthy *et al.* 1994). There is a normal two-fold ambiguity in the location of the spin axis from these methods (see Drummond *et al.* 1985a and Magnusson *et al.* 1989), lying the same angular distance from the asteroid, but in opposite directions. The ambiguity has been resolved for Vesta by repeated observations and fits, but since this is the first such determination for Ceres, the two poles are listed in Table II. A set of similar observations of Ceres on another date will break the ambiguity.

A weighted mean (weights $\propto 1/\sigma^2$) for each of the six parameters found from the two fits is adopted as the best solution and used to find the pole. Table III gives the solution for Ceres and Table IV for Vesta. Figure 7 depicts the fit to the data for Ceres and Figs. 11–13 for Vesta. Uncertainties given in the tables are the errors of the mean between each method for the six parameters according to either the difference between the two methods or the errors assigned to the parameters by the two methods, whichever is greatest. For example, if both methods give the same long axis dimension a, then the uncertainty is not zero, but is based on the uncertainties for a from each method. If a is discordant between both methods, but each gives small

uncertainties for a, then the adopted uncertainty is based on the weighted error of the mean.

5.2. Ceres

Despite being the largest asteroid by far, Ceres has long remained the largest Solar System body without a known rotational pole. Modern asteroid pole determination techniques based on lightcures (Magnusson *et al.* 1989) do not work on Ceres because its lightcurve is always of low amplitude, ≤ 0.04 mag. A spherical or oblate spheroid ($a = b$) shape would produce no lightcurve due to changing cross-sectional area, the usual cause of light variation. If the rotational pole were close to the orbital pole at ecliptic coordinates (351; +79), causing the sub-Earth point to remain close to the asteroid's equatorial plane, then there would be little variation in lightcurve amplitude as Ceres moved along its orbit. Since both phenomena occur (low and non-varying amplitude), it is generally believed that Ceres is near spherical and has a small obliquity—a small angle between its rotational and orbital poles.

Johnson *et al.* (1983) derived a rotational pole at (270; +36) from an analysis of polarized thermal emission. However, the obliquity for this pole (53°) would lead to seasonal
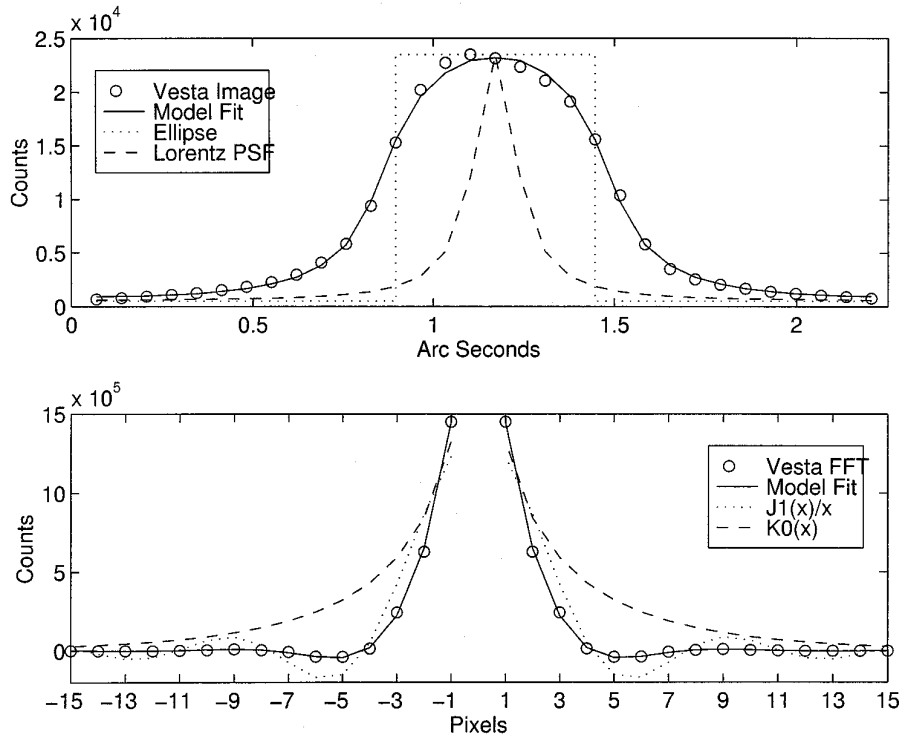
FIG. 5. Same as Fig. 4, but for the observation of Vesta on May 11, 1996, 8:42 UT.

variations in thermal emission, which were not observed by Spencer *et al*. (1989), and large changes in lightcurve amplitudes (if Ceres has a triaxial ellipsoid, and not a spheroidal, shape), which also were not observed. The pole of Johnson *et al*. is 44° from the northern pole in Table II.

Saint-Pe *et al*. (1993) found a pole at (332° ± 5°; +70° ± 15°) from essentially trial and error modeling of 3.6-m telescope COME-ON AO images at multiple wavelengths (*H*, *K*, *L′*, and *M* bands, in particular the latter two which show thermal lag), but only over a small range
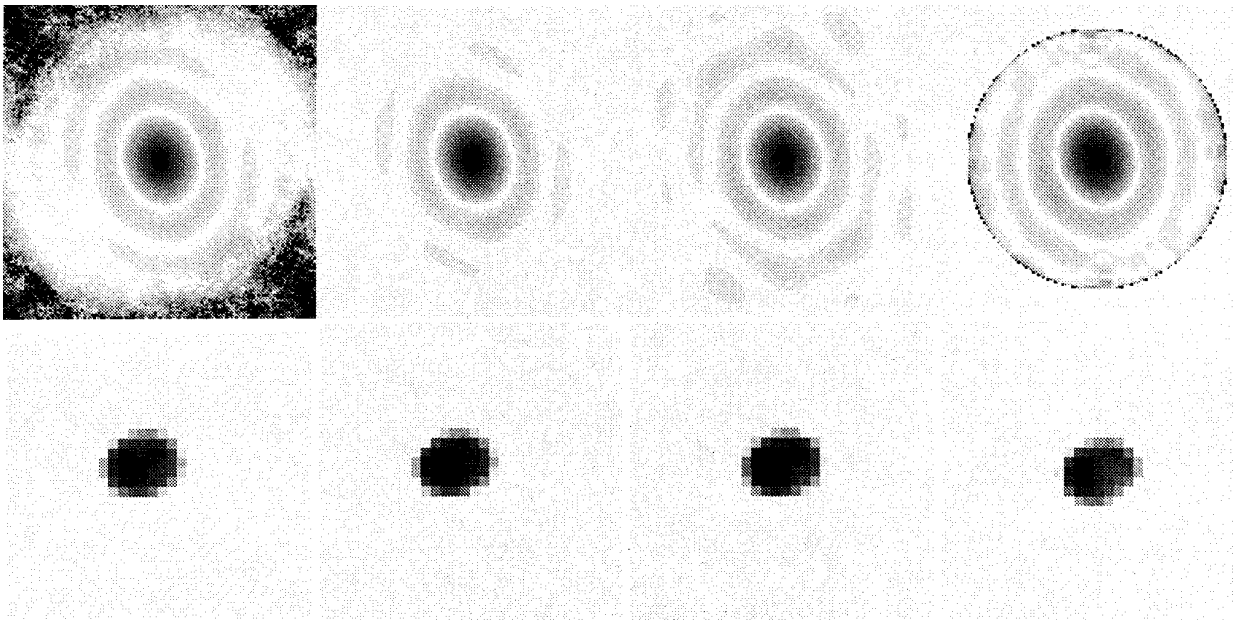

FIG. 6. Comparison of deconvolution techniques. Left to right: Inverse filter, Richardson–Lucy, blind deconvolution, and parametric blind deconvolution. The top row shows the Fourier moduli and the bottom row shows the corresponding diffraction-limited images.

TABLE II
Triaxial Solution for Ceres

Rotational pole (2000.0)	North	South
RA; Dec	280°; +56°	151°; −53°
Long.; Lat.	298°; +78°	186°; −58°
Error radius	3.5°	3.7°
Sub-Earth latitude θ	+14° ± 7°	+15° ± 8°
Rotational phase zero Sep. 19, 1993	9.87 ± 0.17 UT	9.95 ± 0.16 UT
Obliquity ρ	153° ± 1°	329° ± 1°
a	1018 ± 10 km	1014 ± 9 km
b	945 ± 13 km	945 ± 12 km
c	888 ± 10 km	893 ± 10 km

TABLE IV
Triaxial Solutions for Vesta

Rotational pole (2000.0)	Sep. 20, 1993	Apr. 27, 1996	May 11, 1996
RA; Dec	299°; +35°	332°; + 42°	335°; +45°
Long.; Lat.	313°; +55°	355°; +49°	360°; + 50°
Error radius	6.9°	1.2°	0.8°
Sub-Earth latitude θ	−24° ± 14°	+12° ± 4°	+16° ± 2°
Rotational phase zero	5.60 UT ± 0.09	6.65 UT ± 0.05	9.80 UT ± 0.03
Obliquity ρ	8° ± 3°	252° ± 1°	315° ± 1°
a	604 ± 13	563 ± 3	571 ± 2 km
b	539 ± 15	534 ± 3	544 ± 2 km
c	467 ± 25	402 ± 5	434 ± 4 km

of rotational phase. The pole they derive has an obliquity of only 10°, which satisfies thermal and lightcurve histories, and is only 12° from the northern pole in Table II.

The rotational poles in Table II, derived simultaneously with a triaxial shape from the full rotation, have obliquities of only 10 or 21°, also consistent with observation. Although the triaxial shape of Ceres predicts a lightcurve amplitude of up to 0.08 mag, higher than the observed 0.04 mag, the variation in amplitude caused by changing the latitude of the sub-Earth point to 20° above or below Ceres' equator (the maximum possible) is only 0.01 mag. Furthermore, the maximum difference possible between lightcurve maxima due to the maximum excursion of the Earth above and below the equator is 0.008 mag. Thus the pole at either (298; +78) or (186; −58) leads to little variation in lightcurve amplitudes or maximum brightness as Ceres moves around the sky. The predicted maximum equatorial amplitude of 0.08, which is not observed, strongly suggests that Ceres' lightcurve is modulated by hemispheric albedo variations of 4%, some of which appears to visible to the HST (Merline et al. 1996). This does not seem unreasonable for a body as large as Ceres, and gives added impetus for gathering additional AO images.

By fitting the mean albedo or surface brightness of the flat-topped ellipses (found by dividing the total flux in the image by the individual area determinations) to the airmass

at the time, we can make extinction corrections to these relative albedos. (This assumes that albedo contributions are not important or else scatter randomly about a mean asteroid brightness.) Figure 8 shows a lightcurve, for the northern pole, due to the changing cross-section of Ceres from the model (−), and individual measured cross-section area (×) and changing relative albedo or surface brightness (○) points. This decomposition of the lightcurve provides little insight into the discrepancy between the observed 0.04 mag lightcurve and the theoretical 0.08 mag amplitude lightcurve from the triaxial ellipsoid model. Because the three nights' data were not obtained under the best of photometric conditions, apparently Ceres axes were better determined than its albedo.

However, further confirmation of the model of Ceres in Table II is gained by comparing the stellar occultation outline of Ceres from 1984 (Millis et al. 1987) and the 1991 infrared AO image outline of Saint-Pe et al. (1993) with what our model predicts for the time. Unfortunately, a sidereal period for Ceres does not exist and so it is not possible to back-predict to the exact time of the two outlines, but a range of sizes and shapes, corresponding to model maximum and minimum cross-section, can be made for comparison. Table III gives such a comparison, but the most illustrative approach is to draw pictures. Figure 9 shows the predicted range of outlines from the model for the northern pole and the observed outline from the occultation and for the AO image. Since the orientation for the COME-ON image was not given, it is back-calculated from the pole of Saint-Pe et al. along with the assumption of an oblate spheroid. The β predicted position angles in Table III reflect the rocking that the apparent ellipse undergoes during rotation and are not errors. Both figures show that the observations lie within the rotational ranges of the model.

Figure 10 shows the two best images of Ceres, made on September 20 when the Lorentzian PSFs were the smallest, approximately 0.25″. The reconstructed images were produced by PBD—deconvolving the original image by the derived Lorentzian PSF and then convolving this with an
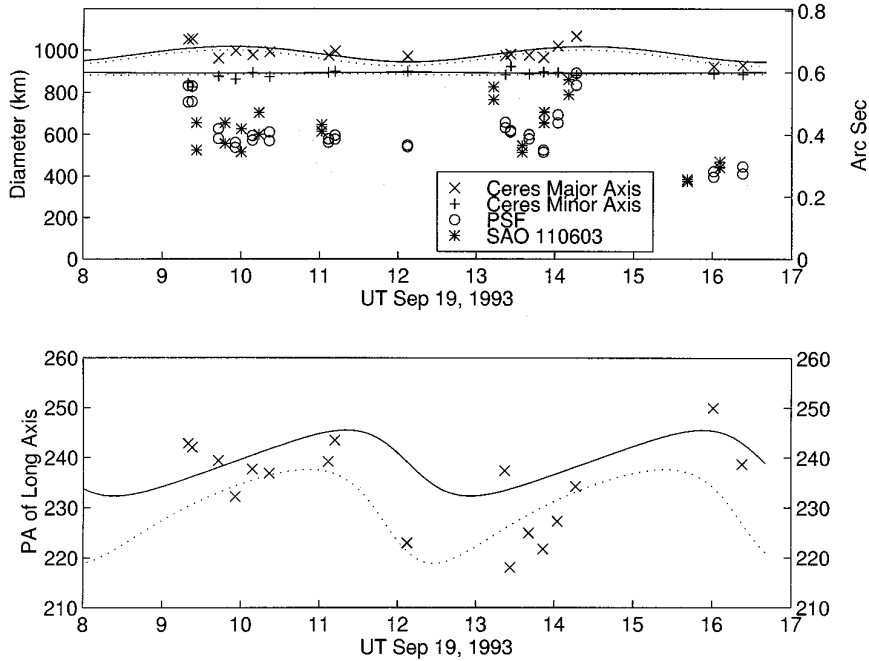
TABLE III
Ceres Projected Ellipse Comparisons

	Occultation predicted ($\theta = +12°$)	Nov. 13, 1984 observed	COME-ON AO predicted ($\theta = -11°$)	May 5, 1991 observed
α	945–1018 km	959.2 ± 4.8 km	945–1018 km	998 ± 41 km
β	894–891 km	906.8 ± 9.0 km	893–890 km	938 ± 39 km
Pos. angle of β	313° ± 6°	331,5° ± 6.2°	34° ± 5°	37° ± 7°

FIG. 7. Plot (upper panel) of the axes diameters of Ceres and of the corresponding Lorentzian point spread functions (PSF), as a function of rotational phase, derived from a simultaneous fit for both. Major and minor axes are distinguished for Ceres, but not for the PSF. Additionally, the diameters of SAO 110603, measured at different times, are indicated by asterisks. The solid lines are the major and minor axes for the illuminated ellipse for the northern pole of Table II, the dashed lines are the same for the terminator ellipse, and the data should fall between the two. The data before 12 UT are from Sep. 19, the data between 12 and 15 UT are from Sep. 18, and the data after 15 UT are from Sep. 20, all folded together with a period of 9.075 h. For the northern pole, the zero phase (indicating maximum cross sectional area) occurs at $10.154 - 0.285 = 9.869$ UT (±0.171 h) on Sep. 19, 1993 (correcting for light travel time), or at $9.948 - 0.285 = 9.663$ UT (±0.156 h) for the southern rotational pole of Table II. The lower panel shows a plot of the position angle of Ceres' major axes, measured from celestial north, as a function of rotational phase.
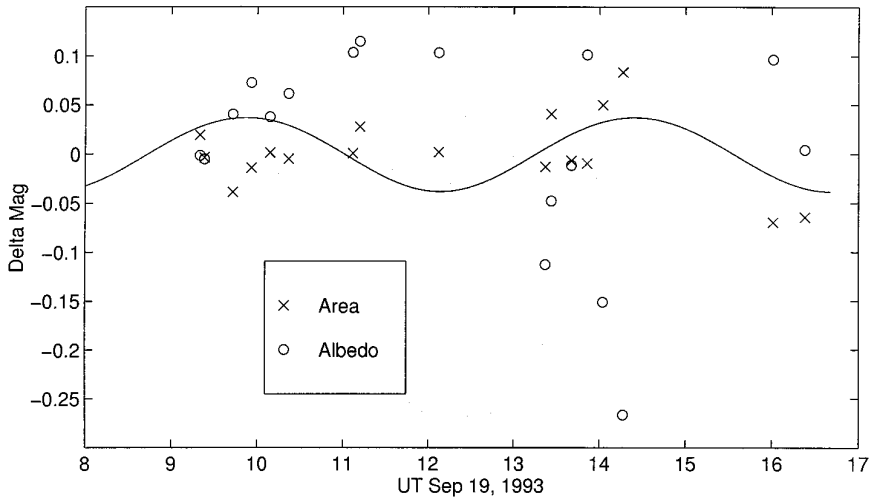

FIG. 8. Plot of Ceres' relative mean albedo (total measured flux divided by area) and cross-sectional area, expressed as relative magnitudes, as a function of rotation for Sep. 19, 1993. The solid line is the area curve, the product of the major and minor radii from the model, and shows an amplitude of 0.08 mag. With no albedo variation, the area curve should generate the lightcurve. There is no obvious trend for the albedo, which leaves unexplained the difference between the theoretical and observed 0.04 mag amplitude lightcurve.
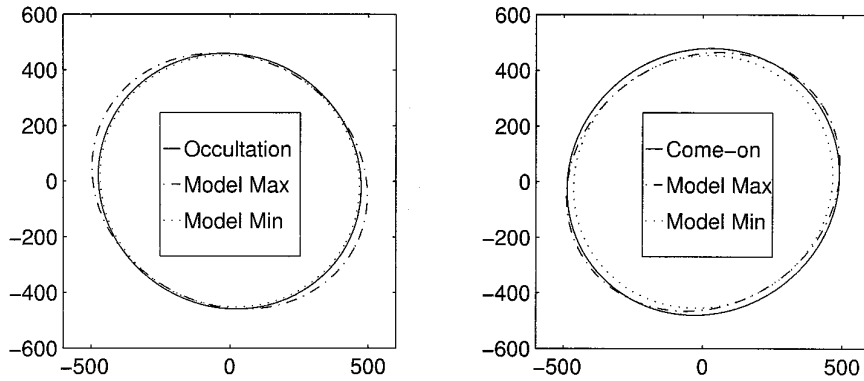
FIG. 9. Comparison of the projection (km) of the triaxial ellipsoid Ceres model to the Nov. 13, 1984 occultation outline and to the image outline obtained by the COME-ON AO system on May 5, 1991. Either pole in Table II produces virtually the same outlines. The orientation of the models could differ from that shown by up to five degrees. Our model's largest and smallest possible outline at the time easily envelope the observed outline. For the occultation the smallest outline most nearly matches the observed ellipse, indicating that the occultation occurred near a minimum in the cross-sectional area.

Airy PSF, as discussed in Section 4. No features can be seen because of the large size of the PSFs—almost one half of the diameter of the asteroid—and thus no markings smaller than this can be expected to be seen. When our 3.5-m telescope comes on line with AO, and as our system improves, we intend to repeat these observations to search for albedo variations across Ceres, as we later show are visible on Vesta.

5.3. Vesta

Vesta has long been known to have major albedo features that dominate its singly periodic lightcurve, as first suggested by Bobrovinoff (1929) and first demonstrated by Degewij *et al.* (1979) with polarimetry. Thus it provides a tempting target for AO. Recent HST images from Vesta's 1994 and 1996 apparitions have verified, in the main, the conclusions from previous indirect (polarimetry, photometry, and reflectance spectroscopy) and direct methods (speckle interferometry), namely that its lightcurve is influenced primarily by albedo markings rather than changing area, and that its face appears non-uniform. In September 1993, Vesta was observed over three nights in lgs mode, but it never rose above an elevation of 35°. On the middle night, despite adequate loop performance for Ceres at
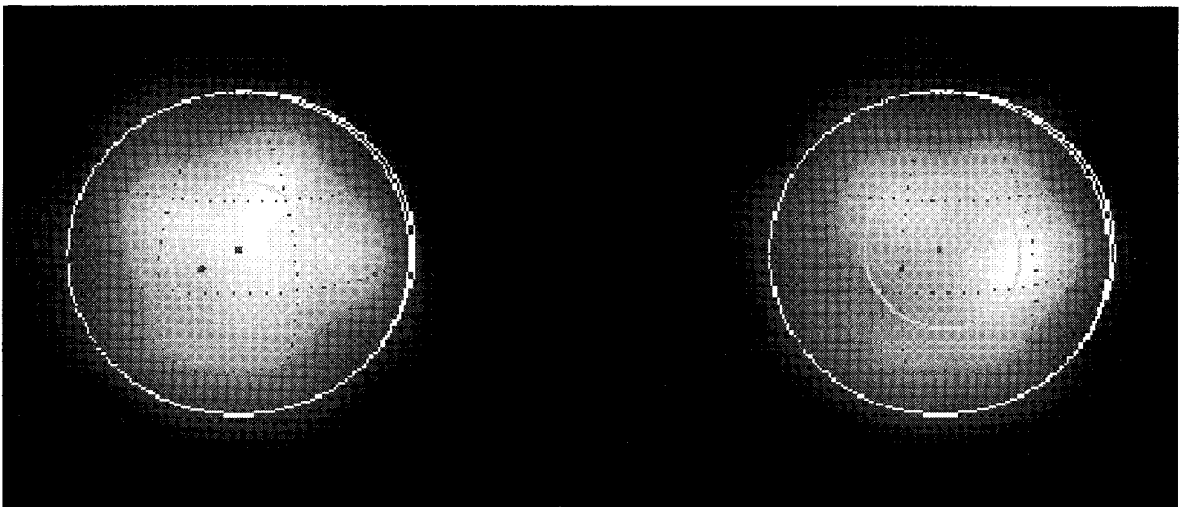

FIG. 10. Reconstructed images of Ceres. The two 60 s observations of Sep. 20, 1993, are deconvolved by the Lorentzian from their fit (the small ellipse in the middle), and then to supress the noise from the deconvolution, filtered by convolving with an Airy PSF that gives a resolution of 0.21″. The outline of the asteroid from the north rotational pole model and the sub-Sun and sub-Earth points are shown, along with lines of latitude at 30° intervals and longitude at 45° intervals. True north lies 31° counterclockwise from the direction of Ceres' north pole, and the Sun another 86° east (counterclockwise). The images are 14° of rotation apart. No features smaller than the PSF can reasonably be expected to be seen.
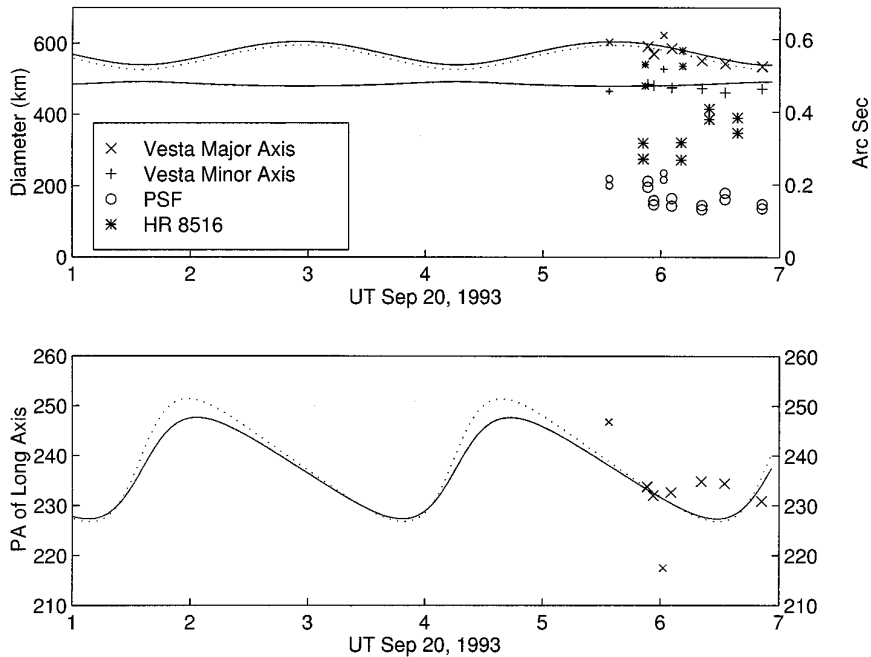
FIG. 11. Same as Fig. 7 upper and lower panels, except for Vesta. (Because the PSFs for Vesta on Sep. 19 are so large, the data are not used in the fit and are not shown.) The Lorentzian point spread functions derived from HR8516 observed between Vesta sets are also depicted. The smaller symbols denote the data from Sep. 18 and the larger ones are the data from Sep. 20 that are used in the least squares fit for the triaxial ellipsoid model for Vesta. Points are folded together with a period of 5.342 h, with the zero phase (indicating maximum cross-sectional area) occurring at $5.797 - 0.195 = 5.602$ UT (± 0.095 h) on Sep. 20, 1993 (correcting for light travel time). All Vesta figures are shown at the same scale for easier comparison.

elevations between 50 and 55°, the PSF was considerably larger than Vesta at lower elevations, rendering diameter measurements useless. However, on September 18 and 20, despite the low altitudes, images were obtained of sufficient quality to allow us to make a determination of Vesta's triaxial ellipsoid shape and the direction of its spin axis. In April and May 1996, we again determined the size, shape, and pole of Vesta, this time in ngs mode, with exceptionally good data from May 11. The results are given in Table IV, and shown in Figs. 11–13.

The AO axial dimensions determined in 1993, and twice again in 1996, continue an interesting trend observed by previous speckle interferometry (SI) results. Table V gives dimensions previously reported and the asterocentric latitude of the phase angle bisector point (PAB), midway between the sub-Earth and sub-Sun points, according to the HST rotational pole at celestial coordinates [301; +41]. The first two entries are from visible SI, the next two are from infrared SI, and the next three are from our AO at a wavelength of 0.85 μm. The HST *adopted* dimensions are also given, as well as the results from their *limb fitting*, the difference being attributed to limb darkening (Thomas *et al.* 1997). Our May 1996 results, with only ~3 km fitting errors, fall midway between the two HST results, and from the *adopted*

results, it appears that good AO techniques underestimate the true axial dimensions by only 1, 3, and 5%, respectively, for the *a*, *b*, and *c* axes.

Figure 14 shows one- and two-parameter weighted fits to the axes' dimensions as functions of the PAB sub-latitude. The left panel is simply a weighted mean, while the right panel shows the relation between *a* and *b* and sin θ, and between *c* and cos θ, which together may indicate the impact of albedo or figure variations on fits which assume a uniform ellipse. The correlation coefficient for the right panel fits are 0.64, 0.68, and 0.70, for *a*, *b*, and *c*, respectively. For Vesta, SI and AO find a greater *a* and *b* when observing over its southern hemisphere than when over its northern and a minimum in *c* when over its equator. On the other hand, ignoring the trends and calculating straight weighted means (left panel) over the years (and over θ) yields axial dimensions gratifyingly similar to the HST results and may indicate that the observed trends are merely caused by one or two peculiar observations. Still, it is not clear whether these trends can be attributed to the observations themselves or should be attributed to Vesta's departure from an ellipsoid figure and/or its albedo variegation.

Table V also lists the coordinates and error radius of the pole from the individual observation sets and compares
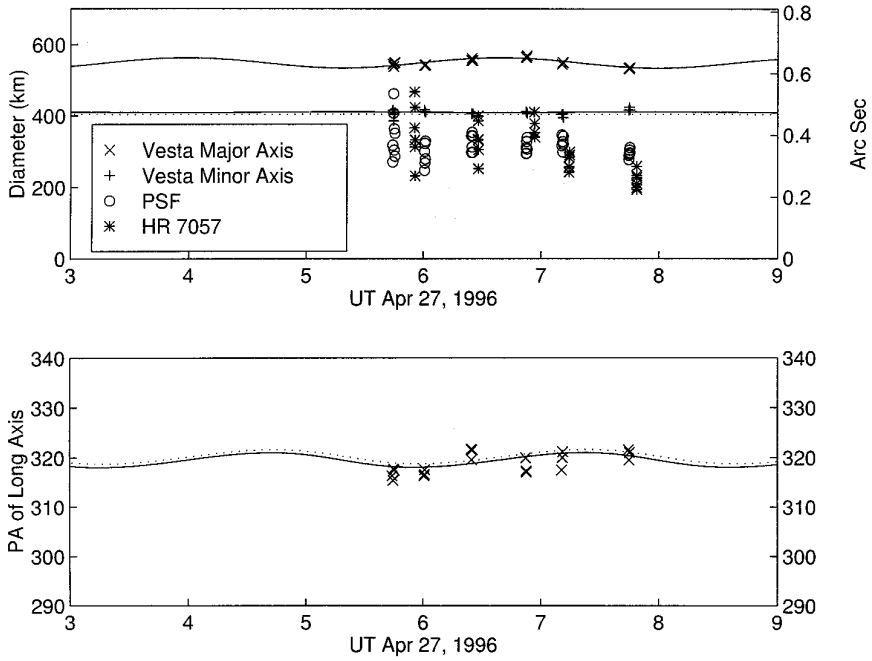
FIG. 12. Same as Fig. 11, upper and lower panels, but for Apr. 27, 1996, and with the point spread function derived from HR7057 observed between Vesta observations. Zero phase occurred at $6.811 - .165 = 6.646$ UT (±0.052) on Apr. 27, 1996 (correcting for light travel time).
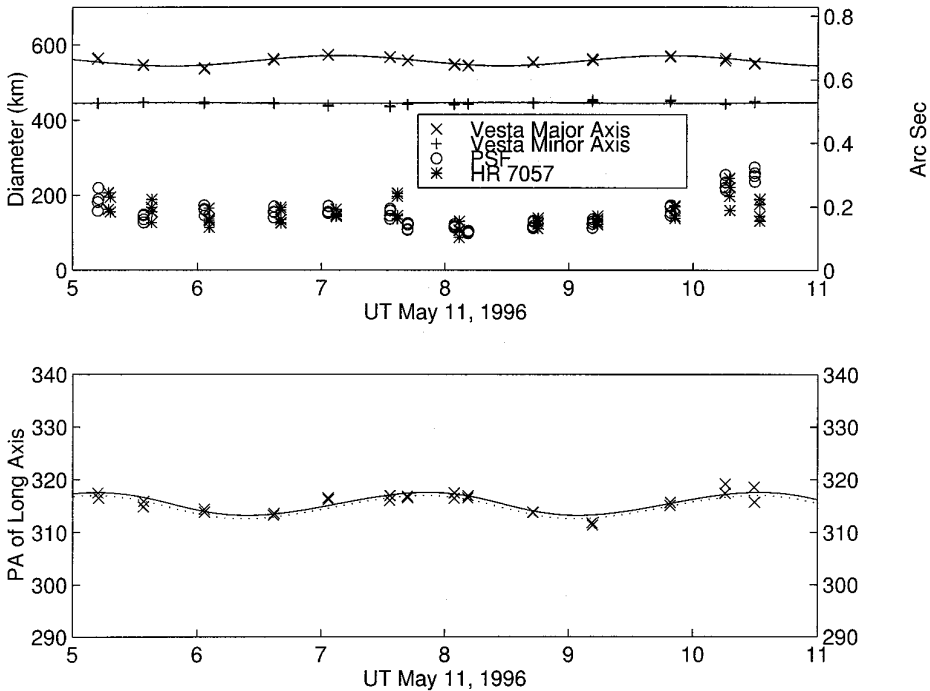

FIG. 13. Same as Fig. 11 upper and lower panels, but for May 11, 1996. Zero phase occurred at $9.966 - .162 = 9.804$ UT (±0.025) on May 11, 1996 (correcting for light travel time). Note how the PSF diameters obtained from HR7057 track with the PSF diameters determined from the asteroid fit. Vesta's diameters do not share the trend, but follow the triaxial ellipsoid curve instead.

TABLE V
Triaxial Dimensions and Rotational Poles from SI and AO

a	b	c	HST θ_{PAB}	Pole (2000) RA	Dec	Err	Date	Method	Reference
584 ± 16	531 ± 11	467 ± 12	+19	315	+41	3.8	Nov. 16, 1983	SI	1
562 ± 14	531 ± 17	466 ± 14	−11	274	+48	7.3	Oct. 14, 1986	SI	2
566 ± 6	528 ± 6	402 ± 8	+8	324	+44	2.2	Nov. 30, 1990	SI IR	3
519 ± 9	486 ± 12	460 ± 8	+19	300	+32	8.4	Feb. 22, 1992	SI IR	3
604 ± 13	539 ± 15	467 ± 25	−21	299	+35	6.9	Sep. 20, 1993	AO	4
563 ± 3	534 ± 3	402 ± 5	−7	332	+42	1.5	Apr. 27, 1996	AO	4
571 ± 2	544 ± 2	434 ± 4	−7	335	+45	0.8	May 11, 1996	AO	4
567 ± 4	539 ± 4	428 + 9		332	+44	6.0		Weighted Mean	
578 ± 12	560 ± 12	458 ± 12	+23	301	+41	5	Nov. 30, 1994	HST Adopted	5
562 ± 12	542 ± 12	426 ± 12	+23	299	+39	10	Nov. 30, 1994	HST Limb Fit	5

Note. References: 1. Drummond *et al.* 1988. 2. Drummond and Hege 1989. 3. McCarthy *et al.* 1994. 4. This paper. 5. Thomas *et al.* 1997.

their weighted average to HST results. Overall, the large scatter is not surprising since the method of finding a pole depends critically on a difference between axes *a* and *b*, i.e., finding the instant when the long axis lies unprojected in the plane of the sky. The 5% difference between *a* and *b* leads to a very small amplitude in Figs. 11–13 (upper panels) for example and presents difficulties in fitting for a pole. Or perhaps the 23° difference between the weighted pole and the HST pole (8° using equal weights), as well as the possible correlation of dimensions with sub-latitude, indicate that Vesta's principle axes of inertia are not aligned with the spin axis.

The fit to the data is so good on May 11, that the relative albedo determinations lead to a good lightcurve decomposition. As for Ceres, we make extinction corrections to the mean surface brightness of the flat-topped ellipses and plot
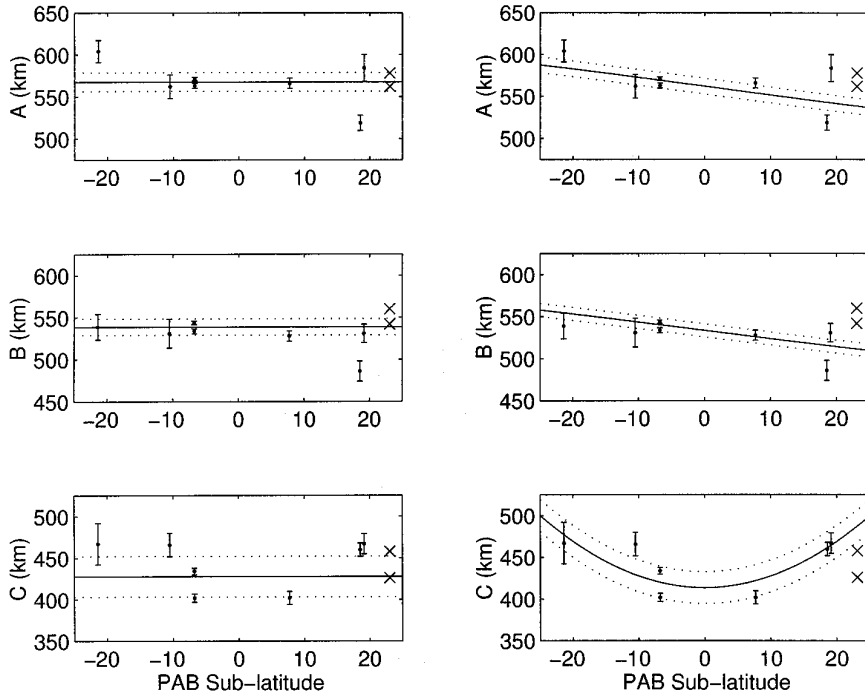

FIG. 14. One (left) and two parameter fits through the derived axes dimensions from speckle interferometry and adaptive optics (Table V) as a function of the phase angle bisector (PAB) sub-latitude calculated from the HST pole at [301; +41]. The adopted (larger) and limb-fitted (smaller) dimensions from the HST results are shown as ×'s. Correlation coefficients for the right panel, from top down, are 0.64, 0.68, and 0.70.
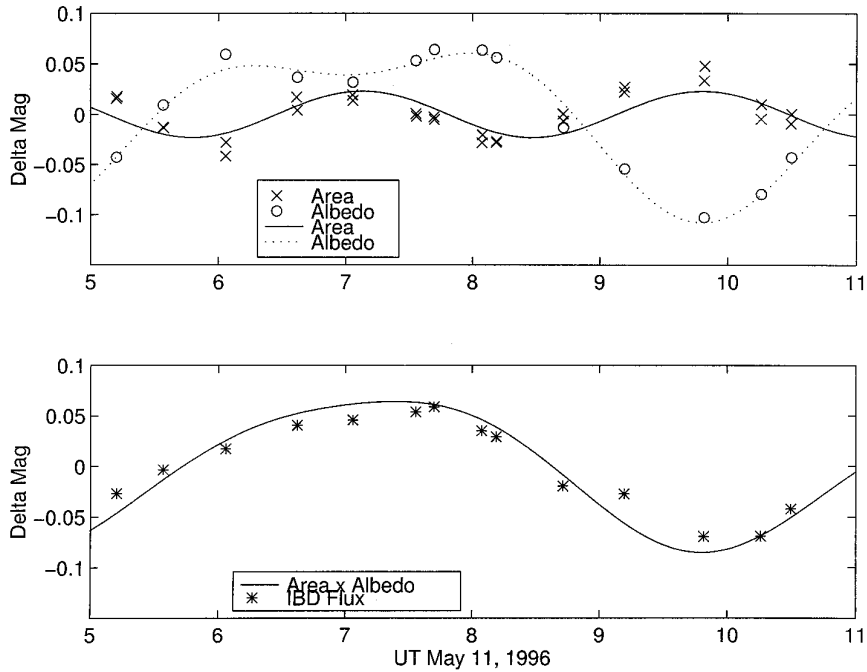
FIG. 15. Plot of Vesta's relative mean albedo and cross-sectional area, expressed as relative magnitudes, as a function of rotation for May 11, 1996. In the upper panel the solid line is the product of the major and minor radii from the model and shows an amplitude of 0.04 mag, while the dashed line is from a second order Fourier fit to the total flux divided by the measured area for one of each pair of observations, with extinction simultaneously taken out. These albedo determinations exhibit an overall amplitude of 0.17 mag. In the lower panel the sum of the area and albedo curves has an amplitude of 0.15 mag, and looks very much like the observed lightcurve of 0.12 mag. The measured total flux (corrected for extinction) from 14 images are shown as asterisks. With no albedo variation, the measured area curve of the upper panel should generate the lightcurve, but instead the minimum in relative albedo occurs close to a maximum in area, confirming what has been known from a variety of techniques, that one dark hemisphere is responsible for Vesta's single maximum/minimum photometric lightcurve.

them against rotational phase. Unlike Ceres, however, a low order Fourier series fit to 14 measured fluxes divided by the corresponding areas, yields a good albedo lightcurve with an amplitude of 0.17 mag, plotted as a dotted line in Fig. 15, along with the triaxial ellipsoid area lightcurve (solid line) with an amplitude of 0.04 mag. Adding them together then produces the predicted lightcurve (lower half of figure), with an amplitude of 0.15 mag, in good agreement with the observed 0.12 mag lightcurve. Thus, from AO images we are able to decompose the contributions to the lightcurve into its cross-sectional area and surface brightness components and verify that indeed one hemisphere is considerably darker than the other, changing what would be a maximum into the minimum of the lightcurve. Our albedo-only lightcurve amplitude of 0.17 mag imples that there is a ~17% variation in overall surface brightness between hemispheres.

Using the time of minimum from 14 photometric lightcurves of Vesta obtained between 1950 and 1990 and applying the method of sidereal photometric astrometry (SPA; see Drummond *et al.* 1988b), we derive a rotational sidereal period for the HST pole at [RA; Dec] = [301; +41] of 0.2225 8873($\pm$0.0000 0004) days. (All times and epochs are corrected for light time travel.) This is comparable to the period derived by Drummond *et al.* (1988a), from one less lightcurve, of 0.2225 887($\pm$0.0000 001) days for their rotational pole at [315; +41], which is only 11° away from the HST pole. As noted above, the SI and AO observations indicate that the times of minimum light occur near maximum projected area. We, therefore, include the seven SI/AO (Table V) rotational phase zero (time of maximum area) determinations with the fourteen lightcurve minima in a new SPA analysis (with the same HST pole). The times of minima are attributed to the asterocentric longitude of the phase angle bisector points, while the times of maximum area from SI and AO are attributed to the longitude of the sub-Earth points. By making a three-parameter fit, we can simultaneously find two separate time zeros for the lightcurve and SI/AO data, and a single sidereal period. This period is similar to the period from lightcurves alone, but with larger uncertainty caused by a large positive and negative residual contributed by the 1986 SI and 1993 AO data. Discarding these two times, we perform the analysis again, finding a period only negligibly different and with a similar uncertainty, 0.2225 8874($\pm$0.0000 0004) days. More telling, we find that the maximum area occurs 6.5° $\pm$ 3.5° after the minimum in the lightcurve. Figure 16 illustrates the fit.
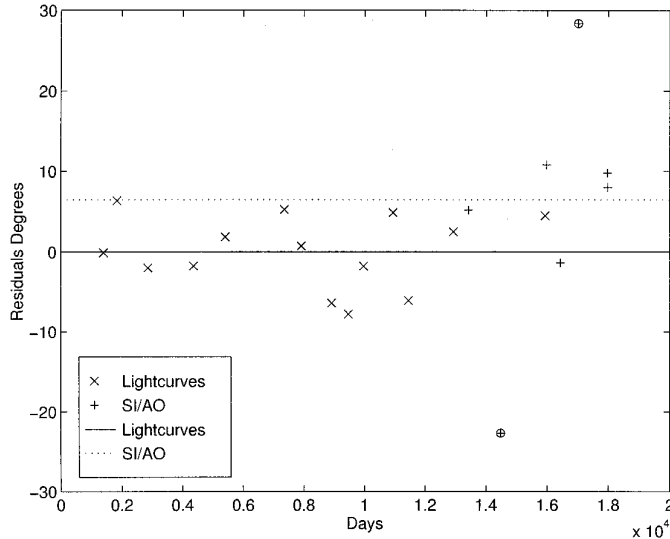
FIG. 16. Residuals, in rotational degrees, of lightcurve minima and adaptive optics/speckle interferometry maximum area for a sidereal period of 0.22258874 days. The different zero points for the two types of data are shown as lines and point to a 6° difference between times of minimum light and maximum area. Circled points were excluded from the fit.

The time of maximum area predicted by Eq. (1) of Thomas *et al.* (1997) is 5.5° later than we observed in May 1996, probably indicating a difference in their time zero point rather than an incorrect period. While their longitude and time zero points are based on a prominent feature, Olbers, which is 10°(±10) in longitude from the long axis *a*, ours (SOR) are based on lightcurve minima and maximum projected area. Thus, for the HST the longitude of the *a* axis is uncertain, while for us the longitude of Olbers is uncertain. To put the two coordinate systems on the same basis, and for intercomparisons, we give the following formulae for predicting the asterocentric sub-Earth longitude (L) on a given Julian data (JD; $JD_0 = 2451545$, January 1.5, 2000), where the Earth's longitude on the date in the inertial coordinate system is k, a function of the RA and Dec of the rotational pole [λ_{pole}; δ_{pole}] and the position of the asteroid [λ_{ast}; δ_{ast}]:

$$L_{HST} = 291.8 + 360(JD - JD_0)/.2225887 - k \quad (1a)$$

$$L_{SOR} = 53.1 - 360(JD - JD_0)/.22258874 + k, \quad (1b)$$

where for

$$\zeta = \arccos[\sin \delta_{pole} \sin \delta_{ast}$$
$$+ \cos \delta_{pole} \cos \delta_{ast} \cos(\lambda_{pole} - \lambda_{ast})], \quad (2a)$$

$$k = \arcsin\left[\frac{\sin \delta_{pole} \cos \zeta - \sin \delta_{ast}}{\sin \zeta \cos \delta_{pole}}\right];$$
$$\text{if } \sin(\lambda_{pole} - \lambda_{ast}) < 0, k = 180 - k. \quad (2b)$$

The sub-Earth latitude is $\theta = \zeta - 90$. The HST sub-longitude is measured west from Olbers and increases with time as the asteroid rotates, but our sub-longitude is measured east from the tip of the long axis and decreases with time. In our coordinate system, the longitude of Olbers is 350 (i.e., Olbers transits when the sub-Earth longitude is 350), the minimum is the lightcurve appears when the longitude of the PAB is 276.5(±2), and the maximum area after the appearance of Olbers occurs at our longitude 270(±5). The relation between the two systems is

$$L_{HST} = -(L_{SOR} + 10), \quad (3)$$

but as indicated above, there is a further 5.5° discrepancy, which may indicate that the longitude difference between Olbers and the tip of the long axis is closer to 15.5° than 10°.

To illustrate, the time of maximum area for Fig. 13 was 9.804 UT on May 11, 1997 = JD 2450214.9085, when Vesta was at [RA; Dec] = [228.5; −6.7]. Using Eq. (2) with the pole at [301; + 41], we find that the asterocentric sub-Earth latitude was −8.6 and k was 16.7. From Eq. (1) we find that in the Olbers-based HST system, the asterocentric sub-Earth longitude was 74.5, while from Eq. (2) it was 270.0 in our axis-based system. Converting the SOR coordinates to HST with Eq. (3) gives an HST longitude of 80.0, indicating a 5.5° difference between HST and SOR. The discrepancy can be resolved by changing 10 to 15.5 in Eq. (3), which makes the longitude of Olbers in the SOR system and the longitude of the tip of the *a* axis in the HST system both 344.5. However, considering the 10° un-
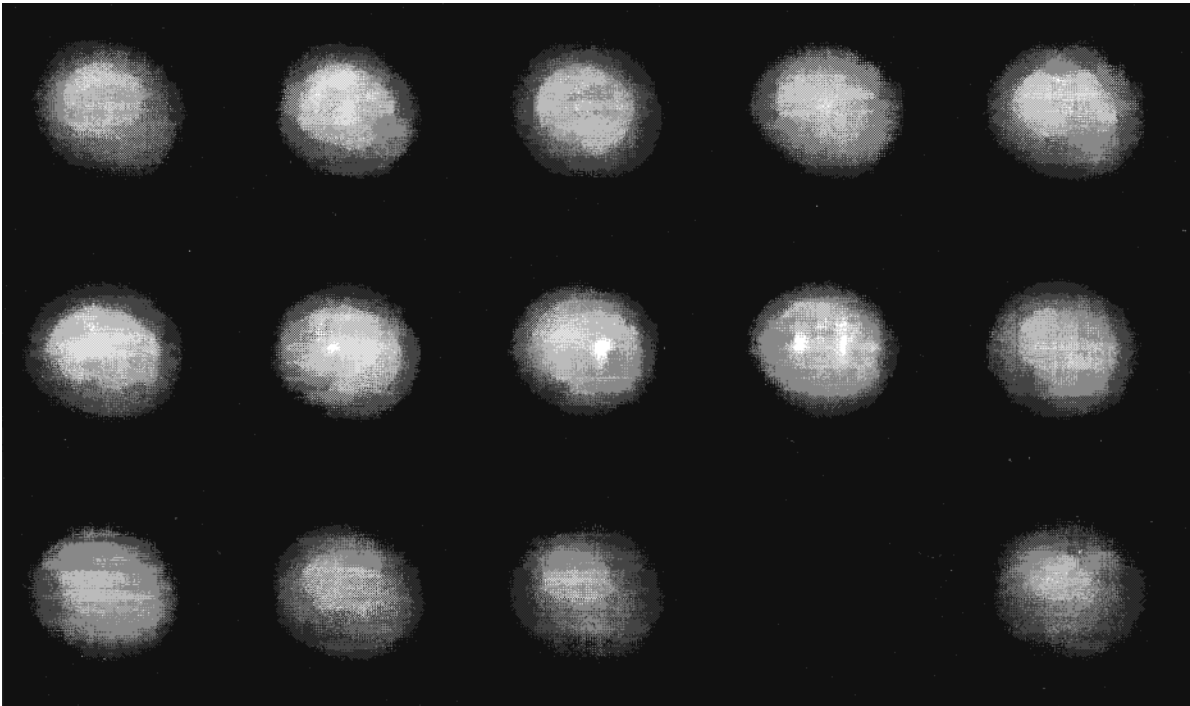
FIG. 17. Vesta's rotation. Read the sequence of IBD reconstructed images left to right, top to bottom. The images are in the same order as Fig. 13, but only one from each pair of observations is shown. The gap marks the end of a rotation. The last image, at the end of the night, is close in rotational phase to the first image from the beginning of the night. The mean brightness of each image corresponds to the asterisks in the lower panel of Fig. 15, showing the change in overall brightness as Vesta rotates. Due to the alt-azimuth mount of the telescope the orientation of celestial north rocks some 15° during the night with respect to the camera, but in general, Vesta's HST north pole lies 22° clockwise from the top of the images, true (celestial) north lies another 47° clockwise, and east is measured counterclockwise.

certainty in the longitude of the long axis with respect to Olbers, and the 5° uncertainty associated with our longitude of maximum area, the 5.5° discrepancy is not much of one. Although this 5.5° difference is assigning longitudes translates to a 4.9 min uncertainty in matching a lightcurve feature to the prime meridian as defined by Olbers, the period remains known to within 3.5 ms, as measured over 74,475 rotations.

Figure 17 is a montage of 14 IBD images of Vesta from May 11, 1996, covering a complete rotation. Each image is convolved with the Airy PSF of the appropriate size derived from the Lorentz and not low pass-filtered with the cosine bell of Eq. (A11) so that they can be compared directly to PBD results. Each reconstructed image is normalized to a volume of unity and then multiplied by the total flux. The sequence is a demonstration of the reason for Vesta's lightcurve—hemispheric albedo variations, not changing cross sectional area. Figure 18 is the same as Fig. 17, but produced by PBD. Each image is first deconvolved with its Lorentzian PSF before convolving with an Airy PSF of the same FWHM and then normalized to the mean surface brightness according to the asterisks in Fig. 15. Figure 19 shows the two best reconstructed images (in the sense of consistent features between consecutive images) of Vesta

from May 11, one just before and one just after 9 UT, 42° later in rotation. The top images have been reconstructed with IBD (filtered with Eq. (A11)) and the bottom images are the same observations reconstructed with PBD. Features that appear in both are likely to be real since the methods of reconstruction are different, with IBD not being restricted to the Lorentzian PSF that constraints each PBD case.

The globes in Fig. 19 are superimposed for the HST pole, but the longitudes are from our axis based system. The circle in the top panel shows the size of the Lorentzian PSF, placed at the HST coordinates of Olbers, [350; +9]. The circle in the bottom panel is placed at our suggested coordinates from the analysis of Vesta's period, [344; +9]. Dark areas are apparent below and along the left side of Olbers. Although in the HST albedo maps, Olbers fades into its surroundings (shows less contrast) between 0.673 and 0.953 μm, it may still be visible at 0.85 μm. With coordinates of [325; −12], the center of the darkest area below and to the left of Olbers transits 35° after minimum cross-section, while the minimum in the albedo lightcurve of Fig. 15 occurs another ~55° of rotation later, at maximum cross-section. From Figs. 17 and 18, we confirm, in the main, what Binzel *et al.* (1997) asserted from mineralogical mapping of the
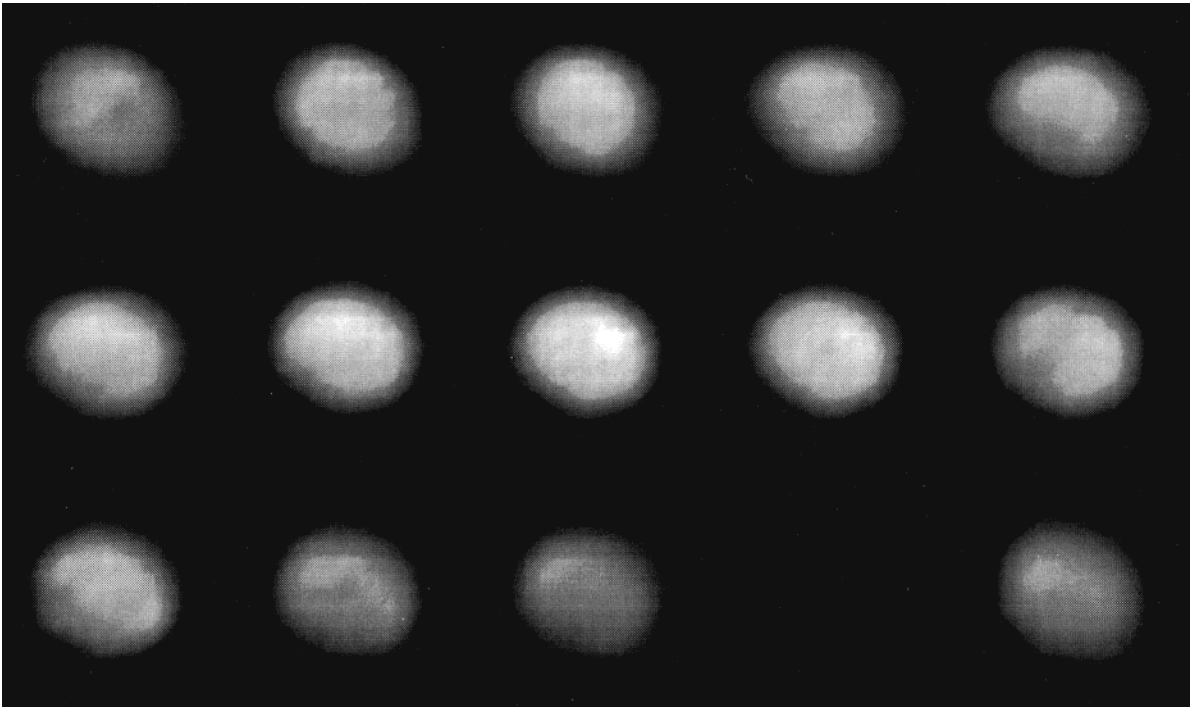
FIG. 18. Same as Fig. 17, except reconstructed images are produced with PBD.

HST images, namely that one hemisphere is darker and less uniform that the other.

6. CONCLUSIONS

We have demonstrated and used a new form of blind deconvolution that constrains the object and the PSF to be analytic functions, thereby allowing parameters of interest to be derived quickly from least squares fits. In our case, asteroids are assumed to be projections of ellipsoids and the PSF for our AO system Lorentzian in shape. The first triaxial shape and rotation pole derived from full rotational coverage for Ceres yields a larger lightcurve amplitude than is observed and implies that hemispheric albedo differences of ~4% may exist. The normal two-fold ambiguity for Ceres' pole is not resolved. One is at a high northern ecliptic latitude and one is at a deep southern latitude. Future similar observations (see below) should break the ambiguity, but a deep southern rotational pole would be somewhat surprising for such a large body. Previous speckle and AO observations of Vesta have been combined to give a model that is reasonably close to that derived from images taken in space by the HST. Vesta's period has been improved a little by combining the SI/AO observations with lightcurves, demonstrating that the minimum in the lightcurve precedes the maximum in cross-sectional area by 6° in rotation or 5.34 min. Some of the albedo structure can be seen with telescopes as small as 1.5 m using adaptive optics.

The future of adaptive optics at the SOR is centered primarily on the 3.5-m telescope. A natural guide star system is nearing first light operation scheduled for the summer of 1997. This system has a goal of achieving Strehl ratios of 0.3 at wavelengths of 1 μm in the natural guide star mode for V = 9–10 objects. It employs a 941 actuator deformable mirror and wavefront sensor running at 1250 frames per second. Laser guide star operation using sodium frequency lasers is also planned for the future.

For even larger telescopes, such as the 6.5-m planned for the University of Arizona, PBD analysis of AO observations will allow, for albedos and contrasts comparable to Vesta, study of asteroids down to ~115 km in diameter at similar precision in the main belt. Since the analysis is performed in the frequency domain, it should be possible to obtain ellipsoid diameters and rotational poles for objects spanning even fewer than the nine to ten pixels we measured for Vesta and Ceres. At four to five pixels, it would be possible to study ~55-km objects in the main belt with a 6.5-m telescope and AO, and since the area of the resolution element on the target scales inversely with the telescope aperture, the brightness per resolution element remains constant, and objects five magnitudes fainter, at V = 11, would be within reach. One intriguing target, for example, is asteroid 216 Kleopatra. From an analysis of its lightcurves, it appears to have an a/c ratio of greater than 3.4 (Drummond *et al*. 1988b, Magnusson *et al*. 1989); and with a mean diameter of 140 km it may be possible to determine whether or not it is a large binary asteroid.
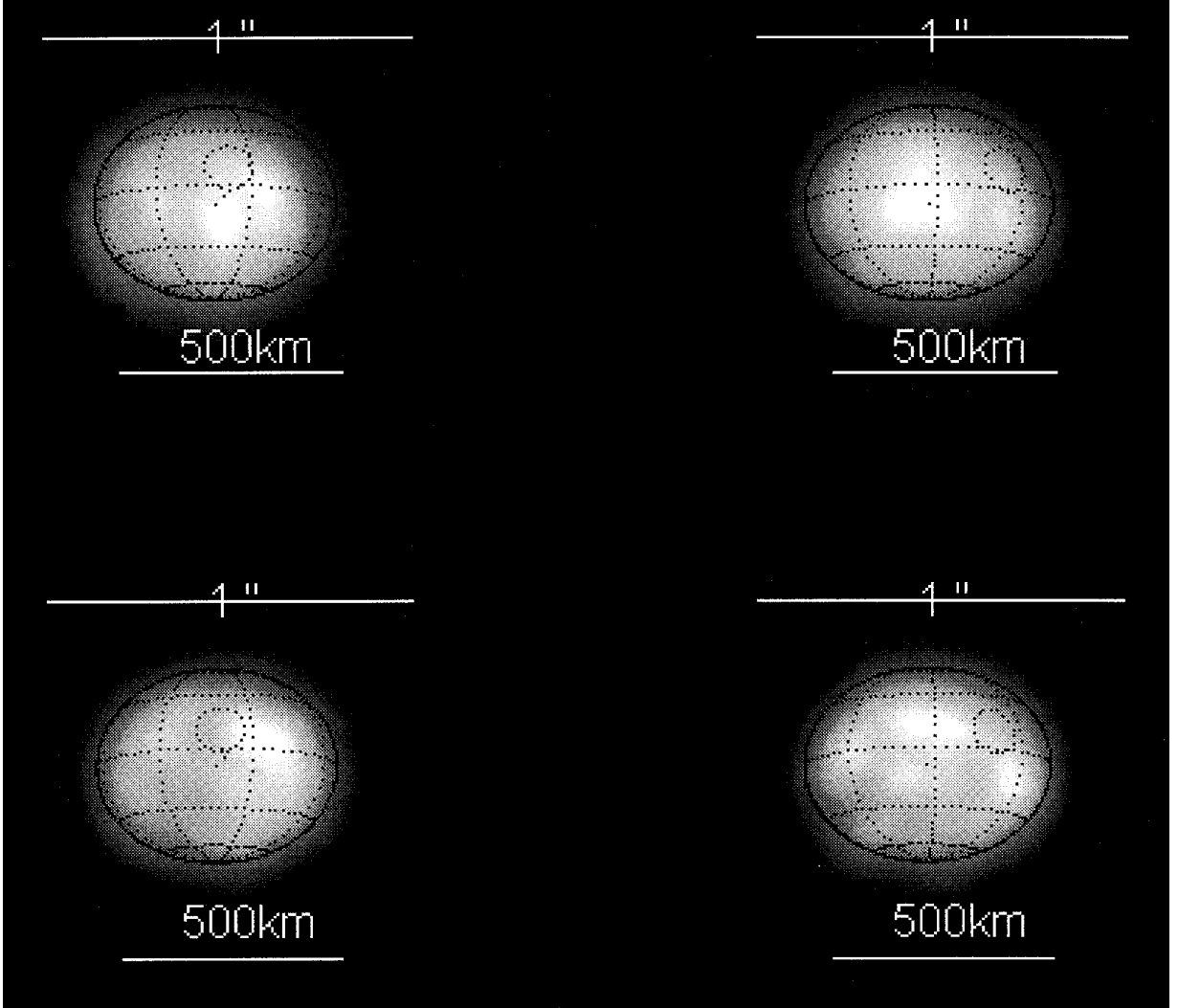
FIG. 19. Reconstructed images of Vesta. The top two images are numbers 10 and 11 in Figs. 17 and 18, reconstructed with IBD, while the bottom are reconstructed with PBD. A dark region runs to the left and south (down) of Olbers, which is marked by a circle (with a diameter of the PSF) placed at the HST coordinates in the upper panel and at our suggested coordinates in the lower panel. Lines of latitude are based on the HST pole, but lines of longitude are in our axis-based coordinate system. True north is 47° clockwise from Vesta's north pole direction, with the Sun coincidently in the direction of true north.

APPENDIX: BLIND DECONVOLUTION IMAGE ANALYSIS

A.1. Parameteric Blind Deconvolution

The general equation for a normalized variable, $r' = r/h$, of an out of round, elliptical distribution function, with semi-axes of α and β and oriented at an angle of ω between α and the X axis, is

$$\left(\frac{r}{h}\right)^2 = \left[\left(\frac{\cos\omega}{\alpha}\right)^2 + \left(\frac{\sin\omega}{\beta}\right)^2\right](x - x_0)^2$$

$$+ \left[\left(\frac{\sin\omega}{\alpha}\right)^2 + \left(\frac{\cos\omega}{\beta}\right)^2\right](y - y_0)^2 \quad (A1)$$

$$+ \sin(2\omega)\left(\frac{1}{\alpha^2} - \frac{1}{\beta^2}\right)(x - x_0)(y - y_0).$$

A Lorentzian is described as

$$L = \frac{A_L}{1 + (r/h)^2}, \quad (A2)$$

where A_L is the amplitude, r is the pixel radius, and since $r'_L = r/h$, h is the elliptical contour of half width at half maximum (HWHM). For our purposes the Lorentzian PSF is parameterized by α_L, β_L, and ω_L.

Making the usual assumptions for an asteroid, namely that it is a smooth, featureless, triaxial ellipsoid rotating about its shortest axis ($a \geq b \geq c$), then its image can be modeled as a flat-topped ellipse, or more accurately, an elliptical cylinder with semi-axes α_E and β_E, oriented at ω_E, and with a height of A_E corresponding to its albedo or mean surface brightness. When the left-hand side (LHS) is equal to unity ($r'_E = r/h = 1$), Eq. (A1) can also be used to describe the asteroid's outline, using α, β, and ω for the asteroid. The intensity distribution in the above-atmosphere image of the asteroid is assumed to be a step function equal to A_E where the pixel radius is less than the RHS of Eq. (A1) ($r/h < 1$) and zero if it is greater. Therefore, four parameters describe the asteroid, α_E, β_E, ω_E, and the mean brightness A_E.

The AO image of the asteroid is then the convolution of a flat-topped elliptical cylinder (the above atmosphere target) and a Lorentzian (the compensated PSF). The Fourier transform ($\mathscr{F}$) of this image is the product of the Fourier transform of the ellipse, E, and the transform of the Lorentzian, L. The former involves a Bessel function of the first kind of order one, J_1, and the latter a Hankel function, specifically a modified Bessel function of the second kind of order zero, K_0, (see Eq. (4) of Section 6.532 in Gradshteyn and Ryzhik 1980). Thus,

$$\mathscr{F}\{E \otimes L\} = \frac{A_E \pi \alpha_E \beta_E 2 J_1(\pi \xi'_E)}{\pi \xi'_E} A_L 2\pi \alpha_L \beta_L K_0(\pi \xi'_L), \tag{A3}$$

where $\otimes$ denotes a convolution and ξ' is the frequency domain normalized variable. Since the Fourier transform of the observation is a product of two analytic functions in the frequency domain, it can be fit with a non-linear least squares routine that solves for the three parameters defining the Lorentzian, the four defining the flat-topped ellipse, and the two locating the image center, x_0 and y_0.

Although the integral of a one dimensional Lorentzian is convergent, the integral of a two dimensional Lorentzian (Eq. (A2)) is not, and thus the center of its transform is infinity, $K_0(0, 0) = \infty$. In the case of the discrete Fourier transform, however, the center pixel in the frequency domain is an integral over the infinity, which yields a finite number:

$$\int_0^{2\pi} \int_0^{R=1/\sqrt{\pi}} A_L 2\pi \alpha_L \beta_L K_0(\pi \xi'_L) r \, dr \, d\theta$$
$$= \frac{A_L 4 \alpha_L \beta_L}{\xi'^2_L} [1 - \sqrt{\pi} \xi'_L K_1(\sqrt{\pi} \xi'_L)]. \tag{A4}$$

K_0 is normalized by this number, giving unit volume for the Lorentzian. The total flux from the image, corresponding to the center pixel in the frequency domain, is thus attributed to the asteroid. In practice, after the normalization, this center pixel is excluded from the fit, which also has the advantage that any flat background residual in the image has no effect in the frequency domain fitting. The asteroid's mean albedo, A_E, can then be found by dividing the flux (determined from either the frequency domain fit or from standard aperture photometry in the image domain) by the area of the ellipse. The derivation of the integral, along with further details, are given by Drummond (1998a,b).

A.2. Iterative Blind Deconvolution

The particular form of IBD implemented here is outlined by the following: Given that $g_k(\vec{r})$ is the kth observation of some object $f(\vec{r})$ at time t_k convolved with a time-variable, space-invariant point spread function $h_k(\vec{r})$, subject to additive noise $n_k(\vec{r})$, the noisy convolution model is

$$g_k = f \otimes h_k + \eta_k s + n_k, \tag{A5}$$

where $s = \mathrm{E}[\hat{s}]$ is the expected sky, or a DC estimate of the non-negative residual to a sky/background calibrated data set, and η_k is a scaling factor. An error metric suitable for conjugate gradient minimization is constructed as

$$\varepsilon_c = \sum_k \sum_{\vec{r} \in S_{c,k}} (\tilde{g}_k - \hat{f} \otimes \hat{h}_k - \eta_k s)^2 \cdot m_k, \tag{A6}$$

where $\tilde{g}_k(\vec{r})$ is the normalized convolution data

$$\tilde{g}_k = \frac{g_k(\vec{r})}{\sum_{\vec{r}} g_k(\vec{r})}, \tag{A7}$$

$\hat{f}(\vec{r})$ and $\hat{h}_k(\vec{r})$ are the object and PSF estimates, respectively, and $m_k = (b_k \cdot w_k)$ is the product of the logical combination of the bad pixel masks and the field-of-view mask b_k, which form the support $S_{c,k}$ over which the convolution error is accumulated, and w_k, the relative weights of the k observations constraining the object and PSF estimates. By normalizing the data and enforcing a normalization constraint on the PSF estimate during minimization, the energy in the object estimate is preserved upon restoration with the normalization factor.

The iterative blind deconvolution utilizes conjugate gradient minimization to find object and PSF estimates $\hat{f}(\vec{r})$ and $\hat{h}_k(\vec{r})$ by minimizing Eq. (A6) subject to further constraints expressing physical properties of convolutions, statistical properties of real data, and any other available *a priori* physical knowledge:

• The PSFs are band-limited. This is enforced by simultaneously minimizing power beyond the diffraction limit of the observation

$$\varepsilon_b = \sum_k^{\mathrm{Frames}} \sum_{|\vec{f}|>f_c} |\hat{H}_k|^2, \tag{A8}$$

where f_c is the aperture cut-off and

$$\hat{H}_k(\vec{f}) = \mathscr{F}[\hat{h}_k(\vec{r})] \tag{A9}$$

is the Fourier spectrum of the PSF estimates $\hat{h}_k(\vec{r})$.

• Real objects and point spread functions are positive definite. This is enforced by estimating both as the squares of corresponding parameters of the minimization $\hat{f}(\vec{r}) = p^2(\vec{r})$ and $\hat{h}_k(\vec{r}) = q_k^2(\vec{r})$.

• Supports are finite. Although a band-limited PSF is infinite in extent, the measurement statistics of real observations limit practical reconstruction to finite domains. Any *a priori* knowledge of physics of the object can also be used for object estimation constraint.

For Vesta the IBD minimization is started with an initial object estimate from the shift-and-add integration of the observed data $\hat{f}(\vec{r}) = \mathrm{SAA}[g_k(\vec{r})]$ and an initial PSF estimate from a corresponding reference star observation similarly shifted and added $\hat{h}_k(\vec{r}) = \mathrm{SAA}[g_{*,k}(\vec{r})]$. To avoid biasing the object estimate by the noise residual in the sky/background subtracted data, the data g_k were offset by a constant such that g_k is everywhere non-negative. That value was used as the initial sky estimate s. The convolution support b_k subtended the region for which $\mathrm{SNR}[g_k] > 1$. The PSFs were adequately supported by a region 64×64 avoiding aliasing in the 128×128 observations. The object support for the hard-limb asteroid data, easily estimated as the half-maximum contour of the shift-and-add estimate $\mathrm{SAA}[g_k]$, was set to a circumscribing circle with radius 1 pixel greater than that contour. Since all of the observations were similar, uniform weighting $w_k = 1$ was used.

The idac algorithm was run 500 iterations for each of 14 sets of observations $\{g_k(\vec{r}); k = 1, 2, 3\}$ of Vesta. We have found that a band-limited linear deconvolution provides further stabilization for the iterative deconvolution process. This gives a new image estimate

$$\hat{f} = \mathscr{F}^{-1} \left[\frac{\sum_k G_k(\vec{f}) \hat{H}_k^*(\vec{f})}{\sum_k \hat{H}_k(\vec{f}) \hat{H}_k^*(\vec{f})} A_b(\vec{f}) \right] \tag{A10}$$

using IBD PSF estimates $\hat{h}_k(\vec{r})$ and a band limit filter $A_b(\vec{f})$, an Airy taper to cut-off $b \leq f_c$. This IBD with "speckle holography" stabilization, Eq. (A10), was iterated three times for each of the 14 data sets. Since objective constraints for limiting the IBD had not yet been implemented, 500 iterations were used, which gave a combination of systematics-free convolution residuals $\varepsilon_c(\vec{r})$ and exponential approach to the noise floor $\varepsilon_c \approx \sum_k |n_k|^2$. Each of the 14 image estimates was then low-pass filtered using a "cosine bell" $C(\vec{f}; f_c/2, f_c)$

$$C(\vec{f}) = \begin{cases} 1 & f \le \dfrac{f_c}{2} \\[2mm] \cos\left\{ \left(\dfrac{2f}{f_c} - 1\right)\dfrac{x}{2} \right\} & \dfrac{f_c}{2} < f < f_c \\[2mm] 0 & f \ge f_c \end{cases} \qquad \text{(A11)}$$

The band-limit filter Eq. (A11) provides a degree of "super-resolution" beyond the optical aperture-tapered diffraction limit without extrapolation beyond measured image frequencies.

ACKNOWLEDGMENTS

REFERENCES

Binzel, R. P., M. J. Gaffey, P. C. Thomas, B. J. Zellner, A. D. Storrs, and E. N. Wells 1997. Geologic mapping of Vesta from 1994 Hubble Space Telescope images. *Icarus* **128,** 95–103.

Bobrovinoff, N. T. 1929. The spectrum of minor planets. *Lick Obs. Bull.* **XIV,** 18–27.

Christou, J. C., B. Ellerbroek, R. Q. Fugate, D. Bonaccini, and R. Stanga 1995. Rayleigh beacon adaptive optics imaging of ADS 9731: Measurements of the isoplanatic field of view. *Astrophys. J.* **450,** 369–379.

Christou, J. C., E. K. Hege, S. M. Jefferies, and C. U. Keller 1994. Application of multi-frame iterative blind deconvolution for diverse astronomical imaging. *SPIE* **2200,** 433–444.

Degewij, J., E. F. Tedesco, and B. Zellner 1979. Albedo and color contrasts on asteroid surfaces. *Icarus* **40,** 364–374.

Drummond, J. D. 1995. Sizes, shapes, and rotational poles of Ceres and Vesta from adaptive optics images. *Bull. Am. Astron. Soc.* **27,** 16.

Drummond, J. D. 1998a. The adaptive optics Lorentzian point spread function. In *SPIE Conference on Astronomical Telescopes and Instrumentation: Adaptive Optical System Technologies*, Kona, HI, March 20–28, 1998.

Drummond, J. D. 1998b. Measuring asteroids with adaptive optics. In *Proceedings NATO ASI, Laser Guide Star Adaptive Optics for Astronomy*. In press.

Drummond, J. D., and E. K. Hege 1986. Speckly interferometry of asteroids. III. 511 Davida and its photometry. *Icarus* **67,** 251–263.

Drummond, J. D., and E. K. Hege 1989. Speckle interferometry of asteroids. In *Asteroids II* (R. P. Binzel, T. Gehrels, and M. S. Matthews, Eds.), pp. 171–191. Univ. of Arizona Press, Tucson.

Drummond, J. D., and J. C. Christou 1994. Adaptive optics images of 1 Ceres, 2 Pallas, and 4 Vesta with adaptive optics at the Starfire Optical Range. *SPIE* **2201,** 468–473.

Drummond, J. D., W. J. Cocke, E. K. Hege, P. A. Strittmatter, and J. V. Lambert 1985a. Speckle interferometry of asteroids. I. 433 Eros. *Icarus* **61,** 132–151.

Drummond, J. D., E. K. Hege, W. J. Cocke, J. D. Freeman, J. C. Christou, and R. P. Binzel 1985b. Speckle interferometry of asteroids. II. 532 Herculina. *Icarus* **61,** 232–240.

Drummond, J. D., J. C. Christou, and R. Q. Fugate 1995. Full adaptive optics images of ADS 9731 and μ Cassiopeiae: Orbits and masses. *Astrophys. J.* **450,** 380–391.

Drummond, J. D., A. Eckart, and E. K. Hege 1988a. Speckle Interferometry of Asteroids. IV. Reconstructed images of 4 Vesta. *Icarus* **73,** 1–14.

Drummond, J. D., S. J. Weidenschilling, C. R. Chapman, and D. R. Davis 1988b. Photometric geodesy of main-belt asteroids. II. Analysis of lightcurves for poles, periods, and shapes. *Icarus* **76,** 19–77.

Drummond, J., R. Fugate, and J. Christou 1996. 1.5 m telescope adaptive optics images of Vesta. *Bull. Am. Astron. Soc.* **28,** 1100.

Dumas, C., and O. R. Hainaut 1996a. First ground-based mapping of the asteroid Vesta. *The Messenger* **84,** 13–16.

Dumas, C., and O. R. Hainaut 1996b. Mapping Vesta with adaptive optics: The 1996 opposition. *Bull. Am. Astron. Soc.* **28,** 1101.

Fugate, R. Q. 1994. Observations of faint objects with laser beacon adaptive optics. *SPIE* **2201,** 10–21.

Fugate, R. Q., C. H. Higgins, B. L. Ellerbroek, J. M. Spinhirne, B. R. Boeke, R. A. Cleis, D. W. Swindle, and M. D. Oliker 1993. *Proc. ICO-16 Sat. Conf. on Active and Adaptive Optics* (F. Merkle, Ed.), pp. 487–492.

Fugate, R. Q., and 15 colleagues 1994. Two generations of laser-guide-star adaptive-optics experiments at the Starfire Optical Range. *J. Opt. Soc. Am. A* **11,** 310–324.

Glenar, D. A., J. J. Hillman, M. LeLouarn, R. Fugate, and J. D. Drummond 1997. Multispectral imagery of Jupiter and Saturn using adaptive optics and acousto-optic tuning. *Publ. Astron. Soc. Pacific* **109,** 326–337.

Gradshetyn, I. S., and I. M. Ryzhik 1980. *Tables of Integrals, Series, and Products* (A. Jeffrey, Ed.). Academic Press, Orlando.

Jefferies, S. M., and J. C. Christou 1993. Restoration of astronomical images by iterative blind deconvolution. *Astrophys. J.* **415,** 862–876.

Johnson, P. E., J. C. Kemp, M. J. Lebofsky, and G. H. Rieke 1983. 10 μm polarimetry of Ceres. *Icarus* **56,** 381–392.

Lagerkvist, C.-I., A. W. Harris, and V. Zappalà 1989. Asteroid lightcurve parameters. In *Asteroids II* (R. P. Binzel, T. Gehrels, and M. S. Matthews, Eds.), pp. 1162–1179. Univ. of Arizona Press, Tucson.

Magnusson, P., M. A. Barucci, J. D. Drummond, K. Lumme, S. J. Ostro, J. Surdej, R. C. Taylor, and V. Zappalà 1989. Determinations of pole orientations and shapes of asteroids. In *Asteroids II* (R. P. Binzel, T. Gehrels, and M. S. Matthews, Eds.), pp. 66–97. Univ. of Arizona Press, Tuscon.

McCarthy, D. W., J. D. Freeman, and J. D. Drummond 1994. High resolution images of Vesta at 1.65 μm. *Icarus* **108,** 285–297.

Merline, W. J., S. A. Stern, R. P. Binzel, M. C. Festou, B. C. Flynn, and L. A. Lebofsky 1996. HST imaging of 1 Ceres. *Bull. Am. Astron. Soc.* **28,** 1101.

Millis, R. L., and 41 colleagues 1987. The size, density, and albedo of Ceres from its occultation of BD + 8°471. *Icarus* **72,** 507–518.

Pennington, T. L., D. W. Swindle, M. D. Oliker, B. L. Ellerbroek, and J. M. Spinhirne 1995. Performance measurements of generation III wavefront sensors at the Starfire Optical Range. *SPIE* **2534,** 327–337.

Roggeman, M. C., B. M. Welsh, and R. Q. Fugate 1997. Improving the resolution of ground-based telescopes. *Rev. Mod. Phys.* **69,** 437–505.

Saint-Pe, O., M. Combes, and F. Rigaut 1993. Ceres surface properties by high-resolution imaging from Earth. *Icarus* **105,** 271–281.

Spencer, J. R., L. A. Lebofsky, and M. V. Sykes 1989. Systematic biases in radiometric diameter determinations. *Icarus* **78,** 337–354.

Thomas, P. C., R. P. Binzel, M. J. Gaffey, B. J. Zellner, and A. D. Storrs 1997. Vesta: Spin pole, size, and shape from HST images. *Icarus* **128,** 88–94.

Zellner, B. J., R. Albrecht, R. P. Binzel, M. J. Gaffey, P. C. Thomas, A. D. Storrs, and E. N. Wells 1997. Hubble Space Telescope images of asteroid 4 Vesta in 1994. *Icarus* **128,** 83–87.